Microscopy image segmentation tool: Robust image data analysis

Ilya Valmianski, Carlos Monton, and Ivan K. Schuller
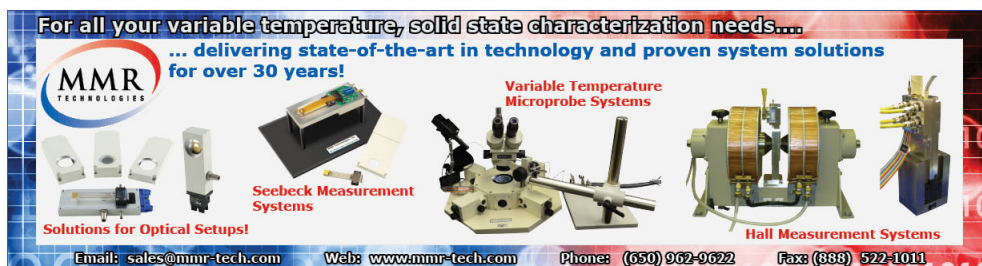
Microscopy image segmentation tool: Robust image data analysis

Ilya Valmianski,[a)] Carlos Monton, and Ivan K. Schuller
Department of Physics and Center for Advanced Nanoscience, University of California San Diego,
9500 Gilman Drive, La Jolla, California 92093, USA

We present a software package called Microscopy Image Segmentation Tool (MIST). MIST is designed for analysis of microscopy images which contain large collections of small regions of interest (ROIs). Originally developed for analysis of porous anodic alumina scanning electron images, MIST capabilities have been expanded to allow use in a large variety of problems including analysis of biological tissue, inorganic and organic film grain structure, as well as nano- and meso-scopic structures. MIST provides a robust segmentation algorithm for the ROIs, includes many useful analysis capabilities, and is highly flexible allowing incorporation of specialized user developed analysis. We describe the unique advantages MIST has over existing analysis software. In addition, we present a number of diverse applications to scanning electron microscopy, atomic force microscopy, magnetic force microscopy, scanning tunneling microscopy, and fluorescent confocal laser scanning microscopy. © 2014 AIP Publishing LLC. [http://dx.doi.org/10.1063/1.4866687]

I. INTRODUCTION

There has been a lot of progress in developing techniques for large area self-assembly of nanostructures.[1–5] These structures have been characterized by scanning microscopy techniques such as Scanning Electron Microscopy (SEM), Atomic Force Microscopy (AFM), and Scanning Tunneling Microscopy (STM).[6–10] Morphological and lattice information extracted from these micrographs are used to understand novel structural, magnetic, and electrical properties. However, most characterizations are only qualitative due to lack of proper tools for uniform and truly quantitative analysis. The main obstacle to developing the necessary tools is the difficulty in effectively segmenting images with large number of regions of interest (ROIs). Many of the most commonly used software packages, such as NIH ImageJ,[11] have only rudimentary segmentation algorithms which are unable to properly analyze complex and often noisy imaging data.

Publications on Anodic Aluminum Oxide (AAO) and nanostructures developed using AAO intermediaries often do not have automated and standardized image analysis. Most often, claims about quality, order, and even size distribution are qualitative and are based on visual examination rather than a set algorithm. Attempts at resolving these problems by introducing a standardized segmentation method have been made, however most of these tools still did not proliferate and often do not feature a convenient interface.[12–14] They generally had disadvantages such as poor segmentation efficiency, inability to find proper region of interest edges, or lack of further quantitative analysis.

In this paper, we present Microscopy Image Segmentation Tool (MIST) which we have developed for periodic nanostructure analysis. This tool provides both an efficient segmentation method for a large number of microscopy problems, as well as analysis tools for morphological and lattice properties of the nanostructures. The tool, written in MATLAB and C++, can be easily integrated with further user-defined analysis, allowing for great flexibility and well defined quantitative results. The software has been packaged in a convenient Graphical User Interface (GUI) and follows an intuitive workflow (Fig. 1). MIST can perform quantitative analysis of a large spectrum of physical, chemical, and biological problems.

II. SEGMENTATION ALGORITHM

MIST uses a robust multistep segmentation algorithm which utilizes both per pixel intensity information as well as morphological filtering. The algorithm makes two assumptions about the underlying imaging data. First, MIST assumes that there is local but not necessarily global contrast between ROI and background. This means that significantly overlapped ROIs are not well segmented however changes in background intensity across the image are corrected. Second, MIST assumes that ROI areas have a Gaussian-like distribution, which is true for most ROI types; however, if the area distribution is multimodal (has many peaks), certain ranges of ROI sizes can be excluded.

The full segmentation algorithm is as follows. For an input image I:

1. Median filter[15] pixel intensity using a 5×5 pixel window.
2. Compute a locally normalized image $\tilde{I}_N$ using a window of size N:

$$\langle I_{x,y} \rangle_N = \frac{1}{(N+1)^2} \sum_{i=x-N/2}^{x+N/2} \sum_{j=y-N/2}^{y+N/2} I_{i,j},$$

$$\langle \sigma_{x,y} \rangle_N = \sqrt{\frac{1}{(N+1)^2 - 1} \sum_{i=x-N/2}^{x+N/2} \sum_{j=y-N/2}^{y+N/2} (I_{i,j} - \langle I_{x,y} \rangle_N)},$$

$$\tilde{I}_{x,y,N} = \frac{I_{x,y} - \langle I_{x,y} \rangle_N}{\langle \sigma_{x,y} \rangle_N}.$$

a)Author to whom correspondence should be addressed. Electronic mail: ivalmian@ucsd.edu
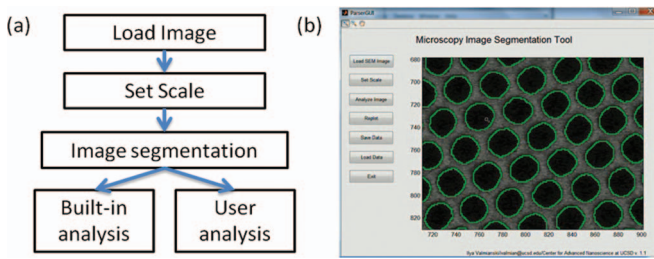
FIG. 1. (a) Data processing flowchart for MIST. (b) Screenshot of MIST after segmentation of a porous alumina membrane fabricated via two-step anodization and pore widening.
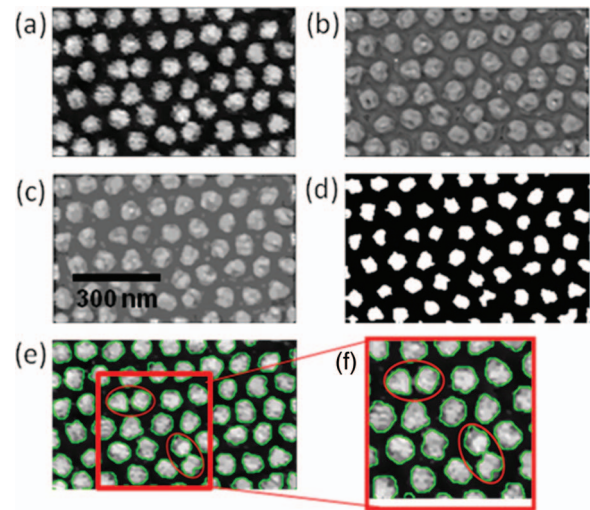

FIG. 2. (a) Raw SEM image of Ni nanodots on Si substrate produced using AAO template. (b) Normalized image (after step 2 in the algorithm). (c) Morphologically filtered image (I_{int} from step 8 in the algorithm). (d) Binary threshold on the morphologically filtered image (after step 9 in the algorithm). (e) Final segmentation (green outlines) superimposed on the raw image. Red ellipses indicate area of minor overlap between nanodots which were nonetheless correctly segmented. (f) Zoom in of (e) showing the overlap between dots.

3. Compute the mean (μI) and standard deviation (σI) of intensities in $\tilde{I}_N$.

4. Threshold $\tilde{I}_N$ at intensities ranging from $\mu I - 3\,\sigma I$ to $\mu I + 3\,\sigma I$ with a step size of $1/2\,\sigma I$ to produce 13 black and white images BW_k.

5. Erode each BW_k with a 3×3 pixel square.

6. Compute the mean (μBW_i) and standard deviation (σBW_i) of the areas of 4-connected pixel groups for each BW_i.

7. Remove all elements from BW_i whose area is more than $3\,\sigma BW_i$ away from μBW_i.

8. Dilate each BW_i with a 3×3 pixel square. If the number of 8-connected pixel groups changes from step 5, go back to step 5. If the number of groups does not change, sum all BW_i to produce a new image I_{int}.

9. Apply manual threshold I_{int} to produce a new image I_f. In practice, the cutoff is usually 7 (corresponding to blocks that have pixel intensities more than μI).

10. Erode I_f with a disk of radius 2.

11. Fill inside 8-connected pixel groups of I_f.

12. Label all 8-connected pixel groups in I_f.

13. Dilate all labeled objects in I_f with a disk of radius 2.

Segmentation is done in two main steps. First, a per-pixel normalization of local intensity (steps 1 and 2).[16] Second, an area-based filtering of normalized regions (steps 3–8). Figure 2 presents a graphical representation of the segmentation algorithm. The algorithm requires three inputs additional to the raw image. First, whether the regions of interest are "dark" or "light." Second, the per-pixel normalization length scale (N). Third, the value at which the final threshold (step 9) is performed.

In the remainder of the paper results using MIST's built in segmentation algorithm will be presented for a variety of physical systems, imagining techniques, and conditions. However, certain problems, such as segmentation of objects with significant overlap or segmentation of a particular class of ROI in an image with multiple similar sized ROI classes, require a more advanced segmentation capability. This can be achieved by users because the segmentation algorithm is written modularly and can be easily changed/replaced while not affecting other MIST capabilities. Important alternative segmentation methods can be derived from erosion,[12] edge detection,[17] watershed transformations,[18] and machine learning techniques.[16]

III. ANALYSIS TOOLS

MIST is used both with built-in and custom user-defined analysis tools. Raw results of the segmentation and of the built-in analysis can be accessed using MATLAB software. Writing additional modules for MIST can also be done in MATLAB. A unique and important feature of MIST is the variety of built-in analysis tools that come with the software (Fig. 3) that are designed to capture parameters commonly cited in the literature on AAO and other self-assembly techniques.

The center-to-center radial two-point correlation function (Fig. 3(f)) describes the long range order of the ROI. Two useful quantities that can be extracted from the correlation function are the nearest neighbor distance, which is the location of the first peak, and the domain size. We estimate the domain size by considering that the correlation functions consist of oscillations due to lattice properties (which we estimate as the standard deviation of the data in a window of size N) and from small random oscillations which are estimated by fitting a model of Additive White Gaussian Noise (AWGN).[19] In particular, we define the domain length scale r as the smallest r for which the following is true:

$$\exp\left(-\frac{(\sigma_{r,N} - \sigma_{AWGN})^2}{2\sigma_{AWGN}^2}\right) > 0.5,$$

where $\sigma_{r,N}$ is the standard deviation in the correlation function values around point r in a window of size N (where N is taken to be 150% greater than the first nearest neighbor) and where σ_{AWGN} is the estimate standard deviation of the AWGN over the entire correlation function.[20]

Region of interest average shape (inset in Fig. 3(a)) displays anisotropies as well as shape distribution of the ROI. Nearest neighbor angle distribution (Fig. 3(c)), together
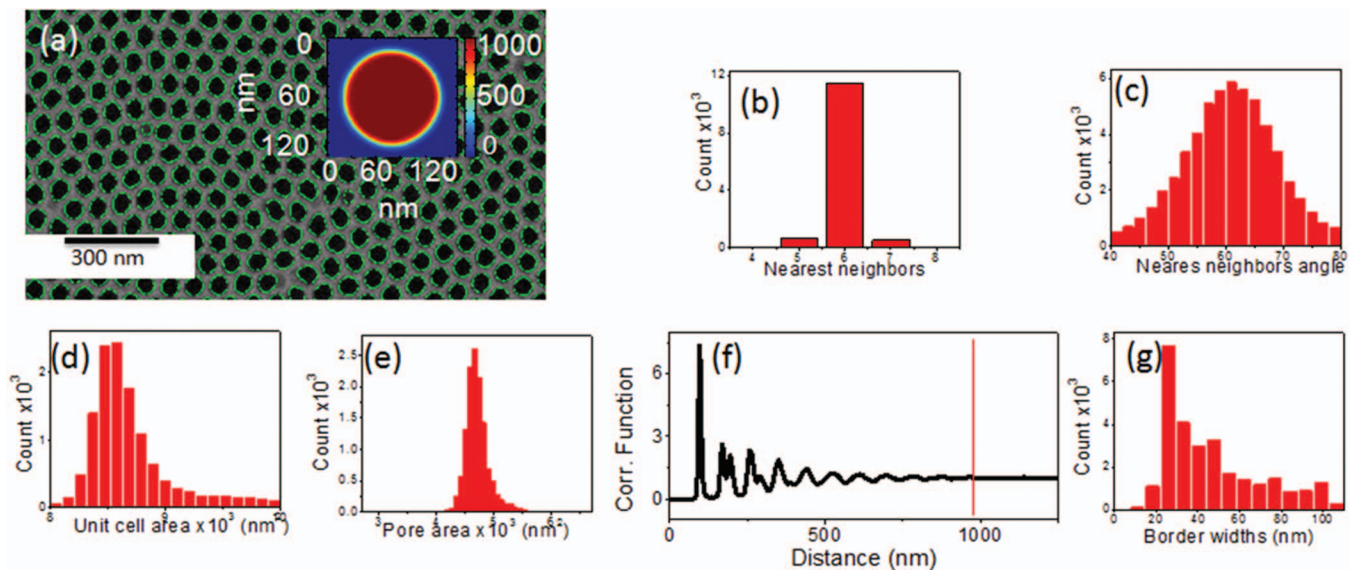
FIG. 3. Analysis of membrane displayed in (a). Green shows automated segmentation while inset shows average pore shape. (b) Nearest neighbor count, (c) nearest neighbor angle distribution, (d) unit cell area distribution, (e) pore area distribution, (f) radial two-point correlation function, and (g) border width distribution. Red line symbolizes the automatically determined length-scale (domain length is 987 nm).

with the radial two-point correlation function, allows comparison to idealized lattice values, which can be used as a "quality" comparison between different samples. Average ROI area (Fig. 3(e)) gives information about ROI size, which is one of the most used values extracted from SEM imaging of self-assembled nanostructures. These values, when extracted manually, tend to be biased by human selection towards what is considered "typical." While this bias is not significant for highly uniform arrays of ROIs, when the ROI size distribution is not symmetric human "experts" often select the most common size as the "mean" rather than the true mean. Furthermore, for non-uniform ROIs different human "experts" may use different personal criteria to find the "mean" values thus making comparison across the literature difficult. Our algorithm presents a completely automatic way of measuring this value and its uncertainty. Unit cell area distribution (Fig. 3(d)) presents information on the uniformity of the lattice. Finally, the number of nearest neighbors (Fig. 3(b)) gives additional information on the "quality" of the lattice.

It is important to note that the ROI at the edges of the image may sometimes bias the statistics. To overcome this, MIST counts edge objects whose size is comparable to those of objects on the inside and discards those that are too small or too big. The two-point correlation function, which is very sensitive to finite size effects, is properly corrected to take into full account the edge effects due to finite image size.

Once the built-in analysis is performed, the raw results together with the per-pixel segmentation data are saved in MATLAB's .mat format. Additional analysis can be applied by loading the .mat file. Most of the parameters needed for these additional analyses, such as ROI labeling, centroid positions, and morphological properties, are already computed during the initial segmentation and are readily available.

IV. EXAMPLE APPLICATIONS

A. Anodic aluminum oxide structures

The original application of MIST was analysis of SEM images of AAO and AAO based nanostructures (Figs. 1–3). AAO membrane templates are used in many applications of large scale nanodot, nanopillar, and antidot fabrication.[21–25] Proper understanding of the nanostructure morphological parameters is critical for designing devices with predictable magnetic properties, superconducting pinning, and metamaterial behavior.[26,27]

Interesting magnetic and electrical properties can be obtained in spatially anisotropic nanostructures.[28,29] Templating such nanostructures using AAO has been an active area of research and led to methods based on selective nucleation, template imprinting, and partial surface occlusion.[30–33] A SEM image and analysis of nanodots generated by electron beam physical vapor deposition (EBPVD) through an asymmetric AAO template are presented in Fig. 4. The template itself was made by depositing a metal layer at 45° to the surface of the membrane, which partially closed the pores. The average pore shape (insets in Fig. 4(a)) can be used to visualize the nanodot anisotropy. The two-point correlation function (Fig. 4(b)) shows that the lattice parameters of the asymmetric dots are the same as that of the parent, symmetric, membrane.

B. Porous silicon

Like AAO, porous silicon has been widely used for molecular confinement and nanostructure templating. It has applications in spectroscopic sensing, battery anode fabrication, and microfluidic devices.[34–37] Fig. 5 presents an example of analysis of porous silicon. SEM of the porous sample and its segmentation is presented in Fig. 5(a). From the two-point correlation function (Fig. 5(b)), it can be seen
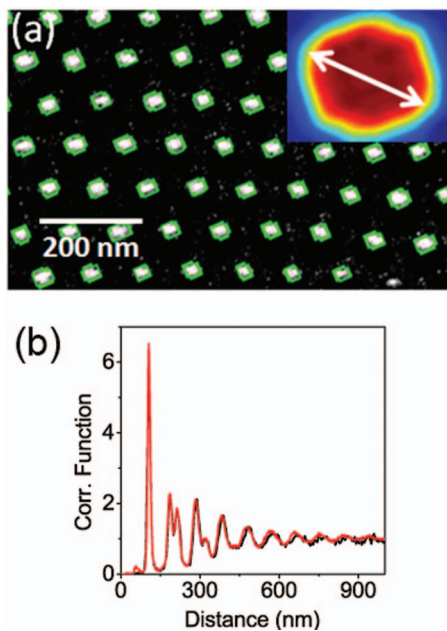
FIG. 4. (a) Segmentation of SEM data of asymmetric Ni dots produced using AAO shadow mask. Inset shows average pore shape, which demonstrates elliptical shape anisotropy. White arrow shows the major axis. (b) Two-point correlation function of the asymmetric nanodot sample (black) and the parent membrane pores (red).

that unlike porous alumina (Figs. 3(f) and 4(b)) porous Si does not have a discernible lattice order. An important parameter in many porous silicon applications is mean wall thickness (Fig. 5(c)). This value is difficult to ascertain manually due to large variance in wall thicknesses and human
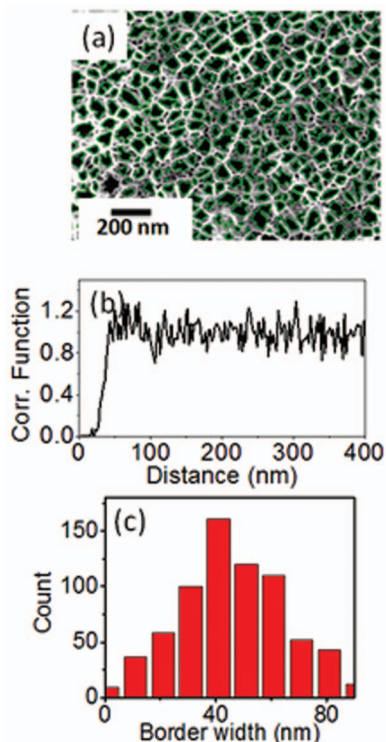

FIG. 5. (a) Segmentation of porous silicon film. (b) Two point correlation function of pore centers. (c) Distribution of border width. (SEM images courtesy of Professor Mike Sailor, UCSD.)

selection bias of "typical" walls. Furthermore, because of large variations in pore sizes and spacing, simply comparing pore average diameter to inter-pore distance is not useful. MIST computes the full wall thickness distribution from which the true mean, median, and standard deviation can be extracted.

C. Vortices in superconductors

Magnetic Force Microscopy (MFM) of vortices in a superconductor can be quantitatively analyzed with MIST. It has been shown that magnetic defects can pin vortices on type II superconductors.[38,39] Much research has been published studying magnetic pinning dependence on defect geometries.[40,41] Control of defect geometry can affect magnetic matching fields, increase superconducting critical current, and change the superconductor's critical temperature.[42] Fig. 6(a) presents MFM micrographs of superconducting vortices on a 100 nm Nb film grown by sputtering on sapphire substrate without addition of pinning sites in a 50 Oe external field. MIST correctly segments individual vortices even though global image contrast is poor. Inspection of the two-point correlation function (Fig. 6(b)) provides the long range
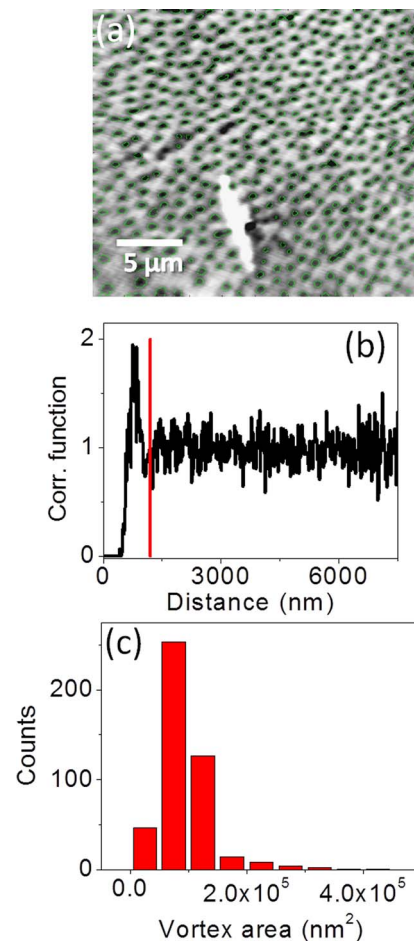

FIG. 6. (a) Segmentation of Magnetic Force Microscopy images of superconducting vortices on 100 nm thick Nb film on Al_2O_3 field cooled at 50 Oe to 2 K. (b) Two point correlation function of vortices (red line indicates domain size). (c) Vortex area distribution. (MFM courtesy of H. Wen, Nanjing University.)
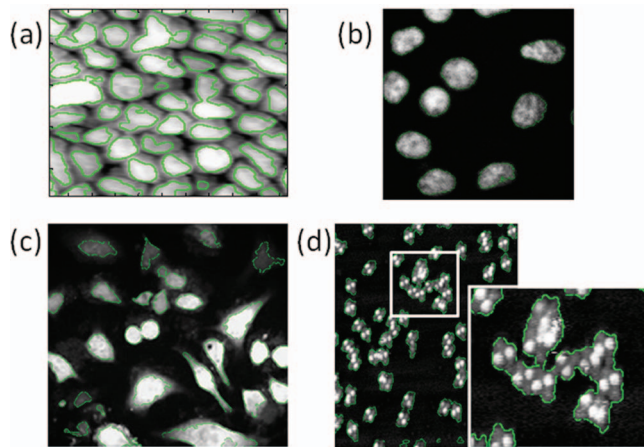
FIG. 7. (a) Segmentation of AFM data on grain structure of 50 nm thick Cobalt Phthalocyanine (CoPc) film. (b) Fluorescent confocal images of Henrietta Lacks (HeLa) cervical cancer cells (image courtesy of S. Sandoval, UCSD). (c) Fluorescent confocal images of neuronal somata and astrocytes. (d) Segmentation of STM images of TCPQ and zoom in on selected region (white square) (image courtesy of C. Urban, UAM, Spain).

characteristics. For example, the nearest neighbor peak is at 750 nm, while ideal close packing predicts 680 nm, similarly, the second nearest neighbor peak is at 1360 nm, while the ideal is 1180 nm. The difference between ideal and the measured values arises because superconducting vortex distribution is strongly mediated by defect pinning. These kinds of precise nearest and second nearest neighbor measurements are very difficult to do manually using NIH ImageJ and similar software because the distribution of nearest neighbors is wide and changes from region to region. A comparison of Fig. 6(b) (vortex distribution) with Fig. 5(b) (pores in Si distribution) shows that unlike a truly disordered sample (porous Si) there is short-range order in the vortex lattice. Finally, analysis of vortex size (Fig. 6(c)) can be used to determine local penetration depth of the superconductor.

D. Biological and organic material

MIST analysis and segmentation capabilities can be applied to a very wide range of applications. For many applications, user-built analysis modules may be used in conjunction with the built-in tools. Fig. 7(a) presents segmentation of an organic film AFM micrograph. These types of images are usually very difficult to segment due to low contrast. Figs. 7(b) and 7(c) show segmentation of a biological sample. These types of images present morphologically diverse regions of interest which require robust morphological filters for proper segmentation. Figure 7(d) presents a STM image of organic molecules. In this example, depending on the final threshold, MIST can be used to segment either the total area covered by the molecules (see figure) or to only select the active lobes (not pictured).

V. CONCLUSION

MIST is a novel and robust segmentation and analysis tool. It can be applied to images produced by a wide variety of techniques, such as Scanning Electron Microscopy, Atomic Force Microscopy, Magnetic Force Microscopy, and Confocal Fluorescent Microscopy. We demonstrate that MIST can be used for physical, chemical, and biological problems. This universality is due to the algorithm's relative insensitivity to overall image contrast and region of interest morphology. The software is highly flexible and can be easily modified to include user-based analysis. This user-based analysis can build on both the segmentation and a large amount of raw information collected about the regions of interest on the image. A copy of MIST, both the source code and a compiled version that does not require MATLAB, can be requested at http://ischuller.ucsd.edu/MIST/.

[1] K. Nielsch, J. Choi, K. Schwirn, R. B. Wehrspohn, and U. Gösele, Nano Lett. **2**(7), 677–680 (2002).

[2] Y. H. Wang and W. D. Zhou, J. Nanosci. Nanotechnol. **10**(3), 1563–1583 (2010).

[3] G. Whitesides, J. Mathias, and C. Seto, Science **254**(5036), 1312–1319 (1991).

[4] R. Maoz, S. R. Cohen, and J. Sagiv, Adv. Mater. **11**(1), 55–61 (1999).

[5] J. J. Gooding, F. Mearns, W. Yang, and J. Liu, Electroanalysis **15**(2), 81–96 (2003).

[6] A. M. Md Jani, D. Losic, and N. H. Voelcker, Prog. Mater. Sci. **58**(5), 636–704 (2013).

[7] M. E. Davis, Nature **417**(6891), 813–821 (2002).

[8] A. Ulyanenkov, J. Chrost, P. Siffalovic, L. Chitu, E. Majkova, K. Erlacher, H. Guerault, G. Maier, M. Cornejo, B. Ziberi, and F. Frost, Phys. Status Solidi A **208**(11), 2619–2622 (2011).

[9] M. Yoon, X. F. Lin, I. Chizhov, H. Mai, and R. F. Willis, Phys. Rev. B **64**(8), 085321 (2001).

[10] Y. Y. Zhu, G. Q. Ding, J. N. Ding, and N. Y. Yuan, Nanoscale Res. Lett. **5**(4), 725–734 (2010).

[11] C. A. Schneider, W. S. Rasband, and K. W. Eliceiri, Nat. Methods **9**(7), 671–675 (2012).

[12] D. S. Raimundo, P. B. Caliope, D. R. Huanca, and W. J. Salcedo, Microelectron. J. **40**(4–5), 844–847 (2009).

[13] H. Kim, R. Maruta, D. Huanca, and W. Salcedo, J. Porous Mater. **20**(2), 375–385 (2013).

[14] K. S. Choudhari, P. Jidesh, P. Sudheendra, and S. D. Kulkarni, Microsc. Microanal. **19**(4), 1061–1072 (2013).

[15] J. S. Lim, *Two-Dimensional Signal and Image Processing* (Prentice Hall, Englewood Cliffs, NJ, 1990).

[16] I. Valmianski, A. Y. Shih, J. D. Driscoll, D. W. Matthews, Y. Freund, and D. Kleinfeld, J. Neurophysiol. **104**(3), 1803–1811 (2010).

[17] J. P. Fan, D. K. Y. Yau, A. K. Elmagarmid, and W. G. Aref, IEEE Trans. Image Process. **10**(10), 1454–1466 (2001).

[18] L. Vincent and P. Soille, IEEE Trans. Pattern Anal. Mach. Intell. **13**(6), 583–598 (1991).

[19] J. Cioffi, *Signal Processing and Detection* http://www.stanford.edu/group/cioffi/book/chap1.pdf.

[20] J. D'Errico, *Mathworks FileExchange* (Mathworks, 2010), http://www.mathworks.com/matlabcentral/fileexchange/16683-estimatenoise.

[21] S. V. N. T. Kuchibhatla, A. S. Karakoti, D. Bera, and S. Seal, Prog. Mater. Sci. **52**(5), 699–913 (2007).

[22] H. Liu, F. Wang, Y. Zhao, J. Liu, K. C. Park, and M. Endo, J. Electroanal. Chem. **633**(1), 15–18 (2009).

[23] G. Schmid, J. Mater. Chem. **12**(5), 1231–1238 (2002).

[24] C. Chiliotte, D. P. Daroca, G. Pasquini, V. Bekeris, C. P. Li, F. Casanova, J. E. Villegas, and I. K. Schuller, Phys. B **404**(18), 2809–2811 (2009).

[25] H. Masuda and M. Satoh, Jpn. J. Appl. Phys. **35**(1B), L126–L129 (1996).

[26] K. Liu, J. Nogues, C. Leighton, H. Masuda, K. Nishio, I. V. Roshchin, and I. K. Schuller, Appl. Phys. Lett. **81**(23), 4434–4436 (2002).

[27] C. P. Li, I. V. Roshchin, X. Batlle, M. Viret, F. Ott, and I. K. Schuller, J. Appl. Phys. **100**(7), 074318 (2006).

[28] S. Y. Chou, Proc. IEEE **85**(4), 652–671 (1997).

[29] R. P. Cowburn, J. Phys. D: Appl. Phys. **33**(1), R1–R16 (2000).

[30] H. Masuda, H. Asoh, M. Watanabe, K. Nishio, M. Nakao, and T. Tamamura, Adv. Mater. **13**(3), 189–192 (2001).

[31] Y. Lei and W. K. Chim, Chem. Mater. **17**(3), 580–585 (2005).

[32] K. Noh, C. Choi, J. Y. Kim, Y. Oh, K. S. Brammer, M. C. Loya, and S. H. Jin, J. Vac. Sci. Technol. B **28**(6), C6m88–C6m92 (2010).

[33] J. Choi, R. B. Wehrspohn, and U. Gösele, Adv. Mater. **15**(18), 1531–1534 (2003).

[34] J. H. Park, L. Gu, G. von Maltzahn, E. Ruoslahti, S. N. Bhatia, and M. J. Sailor, Nat. Mater. **8**(4), 331–336 (2009).

[35] V. Lehmann and U. Gosele, Appl. Phys. Lett. **58**(8), 856–858 (1991).

[36] R. A. Bley, S. M. Kauzlarich, J. E. Davis, and H. W. H. Lee, Chem. Mater. **8**(8), 1881–1888 (1996).

[37] S. O. Meade and M. J. Sailor, Phys. Status Solidi R **1**(2), R71–R73 (2007).

[38] J. E. Zimmerman and J. E. Mercereau, Phys. Rev. Lett. **13**(4), 125–126 (1964).

[39] M. Velez, J. I. Martin, J. E. Villegas, A. Hoffmann, E. M. Gonzalez, J. L. Vicent, and I. K. Schuller, J. Magn. Magn. Mater. **320**(21), 2547–2562 (2008).

[40] V. K. Aksenov, V. I. Sokolenko, and Y. D. Starodubov, Low Temp. Phys. **19**(10), 768–770 (1993).

[41] C. Reichhardt, G. T. Zimányi, R. T. Scalettar, A. Hoffmann, and I. K. Schuller, Phys. Rev. B **64**(5), 052503 (2001).

[42] K. Harada, O. Kamimura, H. Kasai, T. Matsuda, A. Tonomura, and V. V. Moshchalkov, Science **274**(5290), 1167–1170 (1996).